

Chemical Science

Accepted Manuscript

This article can be cited before page numbers have been issued, to do this please use: S. Mondal, M. Salati, M. Nicaso, J. Albero, M. Segado-Centellas, M. Volokh, C. Bo, H. Garcia, M. Gil-Sepulcre, A. Llobet and M. Shalom, *Chem. Sci.*, 2024, DOI: 10.1039/D4SC04678A.



This is an Accepted Manuscript, which has been through the Royal Society of Chemistry peer review process and has been accepted for publication.

Accepted Manuscripts are published online shortly after acceptance, before technical editing, formatting and proof reading. Using this free service, authors can make their results available to the community, in citable form, before we publish the edited article. We will replace this Accepted Manuscript with the edited and formatted Advance Article as soon as it is available.

You can find more information about Accepted Manuscripts in the [Information for Authors](#).

Please note that technical editing may introduce minor changes to the text and/or graphics, which may alter content. The journal's standard [Terms & Conditions](#) and the [Ethical guidelines](#) still apply. In no event shall the Royal Society of Chemistry be held responsible for any errors or omissions in this Accepted Manuscript or any consequences arising from the use of any information it contains.

ARTICLE

Supramolecular interaction of molecular catalyst on a polymeric carbon nitride photoanode enhances photoelectrochemical activity and stability at neutral pH

Sanjit Mondal,^{†[a]} Martina Salati,^{†[b],[c]} Marco Nicaso,^{[b],[c]} Josep Albero,^[d] Mireia Segado-Centellas,^[b] Michael Volokh,^[a] Carles Bo,^{*[b]} Hermenegildo García,^[d] Marcos Gil-Sepulcre,^{*[b]} Antoni Llobet,^{*[b],[e]} Menny Shalom^{*[a]}

Received 00th January 20xx,
Accepted 00th January 20xx

DOI: 10.1039/x0xx00000x

Polymeric carbon nitride (CN) emerged as an alternative, metal-free photoanode material in water-splitting photoelectrochemical cells (PEC). However, the performance of CN photoanodes is limited due to the slow charge separation and water oxidation kinetics due to poor interaction with water oxidation catalysts (WOCs). Moreover, operation under benign, neutral pH conditions is rarely reported. Here, we designed a porous CN photoanode connected to a highly active molecular Ru-based WOC, which also acts as an additional photo-absorber. We show that the strong interaction between the π -system of the heptazine units within the CN to the CH groups of the WOC's equatorial ligand enables a strong connection between them and an efficient electronic communication path. The optimized photoanode exhibits a photocurrent density of $180 \pm 10 \mu\text{A cm}^{-2}$ at 1.23 V vs. reversible hydrogen electrode (RHE) with 89% Faradaic efficiency for oxygen evolution with turnover numbers (TONs) in the range of 3300 and turnover frequency (TOF) of 0.4 s^{-1} , low onset potential, extended incident photon to current conversion, and good stability up to 5 h. This study may lead to the integration of molecular catalysts and polymeric organic absorbers using supramolecular interactions.

Introduction

Polymeric carbon nitride (CN) has gained significant interest as a low-cost and benign photoanodic material for water-splitting photoelectrochemical cells (PEC).¹⁻⁷ However, low charge separation and transfer efficiency and slow water oxidation kinetics hinder the photoactivity and PEC performance of CN photoanodes.⁸⁻¹² Moreover, a pristine CN photoanode is prone to degradation due to the moderate oxygen evolution reaction (OER), which leads to hole accumulation and self-oxidation of the CN layer.^{8,13,14} Therefore, low Faradaic efficiencies (FE) towards molecular oxygen and poor stabilities are usually observed. A common approach to overcome the sluggish OER kinetics in PEC is introducing a co-catalyst, which acts as hole sink and catalytic site for OER.¹⁵ In recent years, only few reports have shown that heterogenous metal oxide-based co-

catalysts can improve the CN photoanode activity towards OER.¹⁵⁻¹⁸ Unlike metal oxide-based photoanodes (BiVO_4 , Fe_2O_3), most known co-catalyst deposition methods did not lead to a successful enhanced oxygen production on a CN-based photoanode.¹⁹⁻²⁴ The poor hole transfer from the CN to the co-catalyst may stem from the insufficient interaction between the materials, although it is still not fully understood. Moreover, CN and many heterogeneous OER electrocatalysts based on oxides work efficiently only in alkaline conditions.^{8,15} Consequently, the performance of CN photoanodes in a neutral electrolyte medium is relatively poor.^{25,26} There is an allure in achieving water-splitting PEC under neutral conditions as it offers gentler operating conditions than alkaline or acidic environments.

Highly performant and robust molecular catalysts have been developed recently for the water oxidation reaction, mainly based on Ru complexes containing the so-called FAME (flexible, adaptable, multidentate, equatorial) ligands that achieve high turnover numbers (TONs) and turnover frequencies (TOFs), with the $[\text{Ru}^{\text{II}}(\text{tda}-\kappa\text{-N}_3\text{O})(\text{py})_2]$ ($\text{Ru}-\text{tda}$, where tda^{2-} is [2,2':6',2''-terpyridine]-6,6''-dicarboxylate and py is pyridine) being one of the best examples.²⁷⁻²⁹ The well-defined nature of these molecular catalysts, together with the capacity to spectroscopically characterize intermediates, have prompted a remarkable development of water oxidation catalysts (WOCs).³⁰ In addition, the capacity to functionalize the ligands that are bonding the metal center, offers a wide variety of anchoring

^[a] Department of Chemistry and Ilse Katz Institute for Nanoscale Science and Technology, Ben-Gurion University of the Negev, Beer-Sheva 8410501, Israel. Corresponding author E-mail: mennysh@bgu.ac.il

^[b] Institute of Chemical Research of Catalonia (ICIQ), Barcelona Institute of Science and Technology (BIST) Av. Països Catalans 16, Tarragona 43007, Spain.

Corresponding author E-mail: cbo@icig.cat, mgl@icig.cat, allobet@icig.cat

^[c] Universitat Rovira i Virgili Av. Països Catalans 35, Tarragona 43007, Spain.

^[d] Instituto Universitario de Tecnología Química CSIC-UPV, Universitat Politècnica de València, València 46022, Spain.

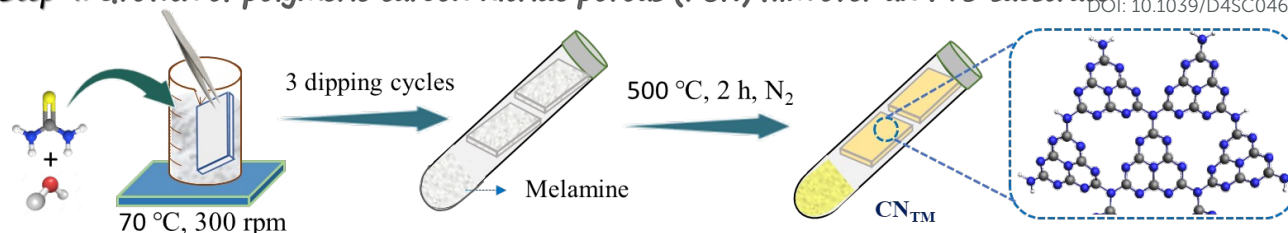
^[e] Departament de Química, Universitat Autònoma de Barcelona Cerdanyola del Valles, Barcelona 08193, Spain.

†Electronic Supplementary Information (ESI) available: Detailed synthesis procedures, characterization, additional figures and tables. See DOI: 10.1039/x0xx00000x

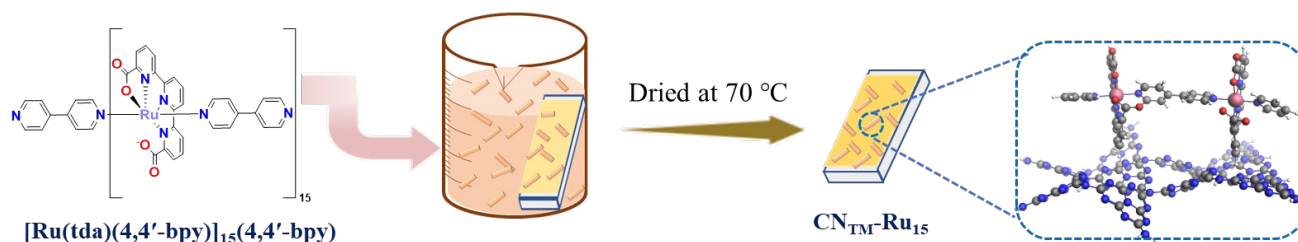
‡ Equal contribution.



Step-I: Growth of polymeric carbon nitride porous (PCN) film over an FTO substrate

View Article Online
DOI: 10.1039/D4SC04678A

Step-II: Modification of PCN surface with Ru₁₅ molecular catalyst



Scheme 1. Procedure for the preparation of CN_{TM} film and the anchoring of the Ru_{15} oligomer to generate the hybrid material $\text{CN}_{\text{TM}}\text{-Ru}_{15}$.

strategies.^{31–35} Recently, we have developed the oligomeric derivative of the Ru-tda catalysts, using 4,4'-bpy as bridging ligands to form $[\text{Ru}(\text{tda})(4,4'\text{-bpy})]_{15}(4,4'\text{-bpy})$ (Ru_{15}).³⁴ The latter has the capacity to generate a large number of CH- π interactions with graphitic surfaces, generating robust hybrid materials for the efficient oxidation of water in heterogeneous phase.

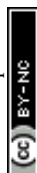
In the present work, we explore the capacity of the Ru_{15} catalyst to interact with the π system of the heptazines, constituting the repeating unit of the CN material, via the CH groups of the tda ligand and generating a monolayer of well-defined molecular catalyst on top of the CN surface. The CN synthetic procedure is chosen to form a porous layer with good adhesion to the conductive substrate (i.e., fluorine-doped tin oxide, FTO), allowing exploration of the co-catalyst role on an FTO/CN/ Ru_{15} photoanode. This should provide the needed electronic communication between the co-catalyst and the light absorbing material, leading to a superior performance of the hybrid material constituted by Ru_{15} and the CN.

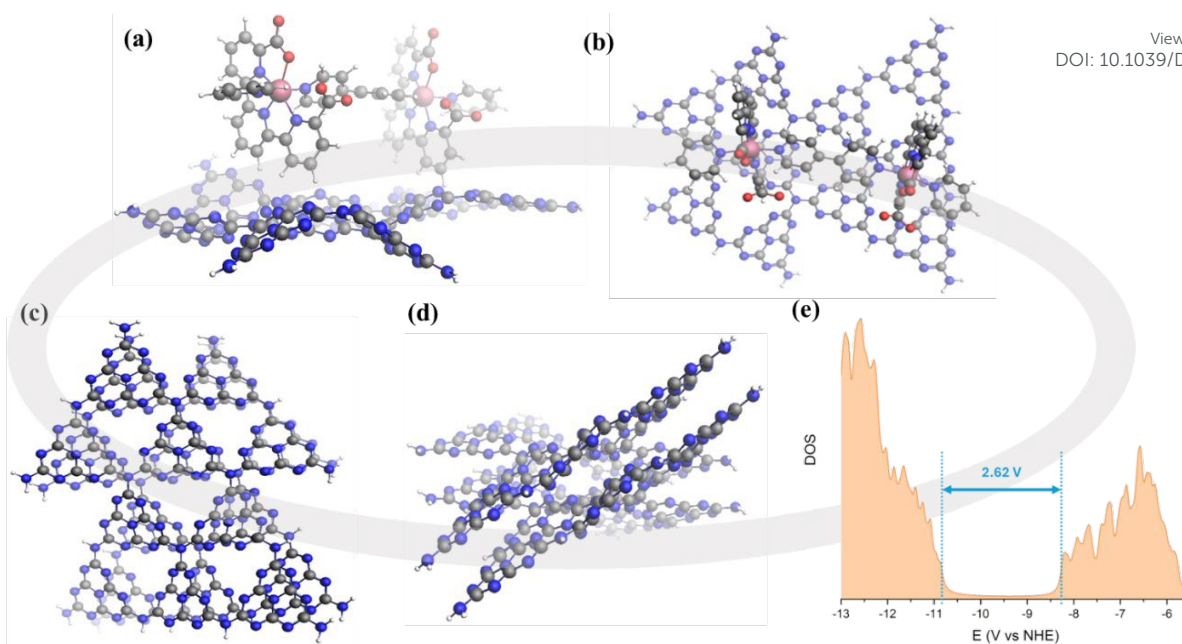
Results and discussion

The fabrication process of a porous CN film over FTO-coated glass as the substrate is illustrated in Scheme 1. Thiourea and melamine were used to prepare CN_{TM} photoanodes using a two-step method involving dipping and thermal treatment. The anchoring of the Ru_{15} oligomer into the CN_{TM} film was performed by dipping the CN_{TM} electrode in a solution containing 1 mg of Ru_{15} in 10 mL of 2,2,2-trifluoroethanol (TFE), for 20 min. Afterward, the electrode was removed from the solution and rinsed with TFE to generate the hybrid material, $\text{CN}_{\text{TM}}\text{-Ru}_{15}$. Further experimental details are given in the Supporting Information. The interaction of the Ru_{15} oligomeric water oxidation catalyst with the surface of the CN film occurs via CH- π interaction, as we have previously described in the

case of graphitic surfaces.^{34–36} In order to further characterize this interaction and visualize it, we have carried out DFT calculations with a low molecular weight model system that involves a 10 heptazine units (164 atoms: 60 C, 86 N, and 18 H) molecule for the carbon nitride, labelled as CN_{Red} , and a dinuclear Ru complex $\{[\text{Ru}(\text{tda})(\text{py})_2(\mu\text{-}4,4'\text{-bpy})]\}$ labeled as Ru_2 , to form $\text{CN}_{\text{Red}}\text{-Ru}_2$ (See Fig. 1, Fig. S14–S22 and Tables S4–S7[†]). Structural combinations of the two units were explored, including aqueous solvent effects, yielding, for the most favorable case, a stabilization energy of 12.7 kcal mol⁻¹ per Ru center, which would imply 190.5 kcal mol⁻¹ for the entire Ru_{15} oligomer with CN_{TM} . This large stabilization energy is due to CH- π interactions between the CH aromatic groups of the tda ligands bonded to the Ru center and the π -system of the CN_{Red} surface.

XRD (X-ray diffraction) and FTIR (Fourier-transform infrared) spectroscopy were used to investigate the structural and functional properties of the films. The CN_{TM} material exhibits two characteristic diffraction signals at 13.0° and 27.4°, which can be assigned to (100) and (002) planes, respectively, representative of the interplanar spacing and the conjugated aromatic system (Fig. 2a) in a heptazine-based CN.^{37,38} Upon the incorporation of the Ru_{15} oligomeric catalyst, the XRD pattern remains unchanged, underlining the structural stability of CN_{TM} films. The FTIR spectra of CN_{TM} and $\text{CN}_{\text{TM}}\text{-Ru}_{15}$ films show the typical peak at 805 cm⁻¹, which corresponds to the breathing mode of triazine units present in the sample (Fig. 2b). Additionally, stretching modes of CN heterocycles were observed between 1200 to 1600 cm⁻¹, with specific vibrations at 1400 and 1633 cm⁻¹ in the CN_{TM} film. Upon loading of Ru_{15} catalyst onto the CN_{TM} film, the stretching modes of the CN heterocycles are found to be 1394 and 1625 cm⁻¹. The broad band observed between 2980 and 3500 cm⁻¹ in the spectra is





View Article Online
DOI: 10.1039/D4SC04678A

Fig. 1 (a) Side and (b) top views of the DFT calculated model of $\text{CN}_{\text{Red}}\text{-Ru}_2$. (c) Top and (d) side views of optimized structure consisting of two layers of heptazine units ($\text{CN}_{\text{Red}})_2$ interacting via π - π stacking interactions. (e) Density of States diagram for ($\text{CN}_{\text{Red}})_2$.

attributed to either NH_2 groups or surface-adsorbed water molecules.³⁸ Additionally, ^1H NMR, XRD, and FTIR data of the Ru_{15} oligomer are provided in Fig. S1†.

The modification of the CN_{TM} film with Ru_{15} oligomer has caused a visual change in the electrodes (Fig. 2c), which translates in the presence of a new broad band at approximately 480–550 nm, associated with metal to ligand

charge transfer (MLCT) band for the Ru complex, as can be observed in the diffuse reflectance spectrum (DRS) in Fig. 2d, and is comparable to the one visible in the UV–vis spectrum of Ru_{15} (Fig. S2†).

The direct optical bandgaps (E_g) of the CN_{TM} and $\text{CN}_{\text{TM}}\text{-Ru}_{15}$ films are 2.61 and 2.50 eV, respectively (Fig. S3†). Valence band X-ray photoelectron spectroscopy (VB-XPS) discloses a more positive VB energy (E_{VB}) position for the $\text{CN}_{\text{TM}}\text{-Ru}_{15}$ films of 2.17 V vs. NHE with regard to that of bare CN_{TM} which gives a value of (1.97 V vs. NHE) and thus a better thermodynamic driving force for the former (Fig. S4†).^{10,38} Finally, the corresponding conduction band energy (E_{CB}) of the CN_{TM} and $\text{CN}_{\text{TM}}\text{-Ru}_{15}$ films are -0.64 and -0.33 V vs. NHE, respectively (inset of Fig. 2d for the energy diagram).

The electronic properties of the CN_{TM} material were also analyzed based on TD-DFT calculations. A single sheet of CN_{Red} made out of 10 heptazine units gave a band gap of 3.25 eV. Interestingly, a two-layer of heptazine units ($\text{CN}_{\text{Red}})_2$ interacting via π - π stacking, as shown in Fig. 1, gives a band gap of 2.62 eV closely matching the experimental value (2.61 eV), thus manifesting the importance of the delocalization of the electron density on the 2D network along with the π - π stacking interactions among the different layers to properly describe carbon nitride type of materials.

Photoluminescence (PL) spectra are significantly different in the presence and absence of the Ru_{15} as can be observed in Fig. 2e, where the intensity of the prominent emission peak at 450 nm in the $\text{CN}_{\text{TM}}\text{-Ru}_{15}$ is partially quenched compared to pristine CN_{TM} , suggesting the presence of an alternative non-radiative recombination path.^{39,40}

SEM images of the CN_{TM} (Fig. 3a) indicate a porous sheet-like morphology with good adhesion to the FTO substrate with

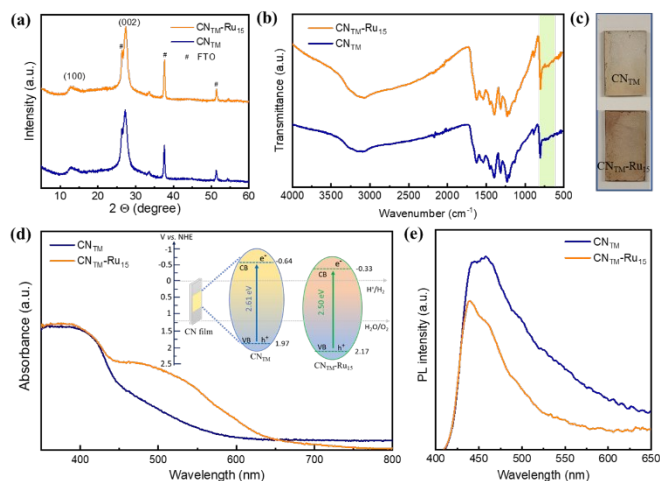


Fig. 2 (a) XRD of CN_{TM} and $\text{CN}_{\text{TM}}\text{-Ru}_{15}$ films over FTO-coated glass. (b) FTIR spectra of CN_{TM} and $\text{CN}_{\text{TM}}\text{-Ru}_{15}$ films. Spectra are vertically offset for clarity. (c) Digital photographs of CN_{TM} and $\text{CN}_{\text{TM}}\text{-Ru}_{15}$ photoelectrodes on FTO. (d) UV–vis DRS of CN_{TM} and $\text{CN}_{\text{TM}}\text{-Ru}_{15}$ films. Inset is the Schematic representation of the electronic band structure of CN_{TM} and $\text{CN}_{\text{TM}}\text{-Ru}_{15}$ (on the normal hydrogen electrode (NHE) scale) determined using the XPS-VB position and the optical E_g calculation. (e) Photoluminescence emission spectra (excitation wavelength 370 nm) of CN_{TM} and $\text{CN}_{\text{TM}}\text{-Ru}_{15}$ films.



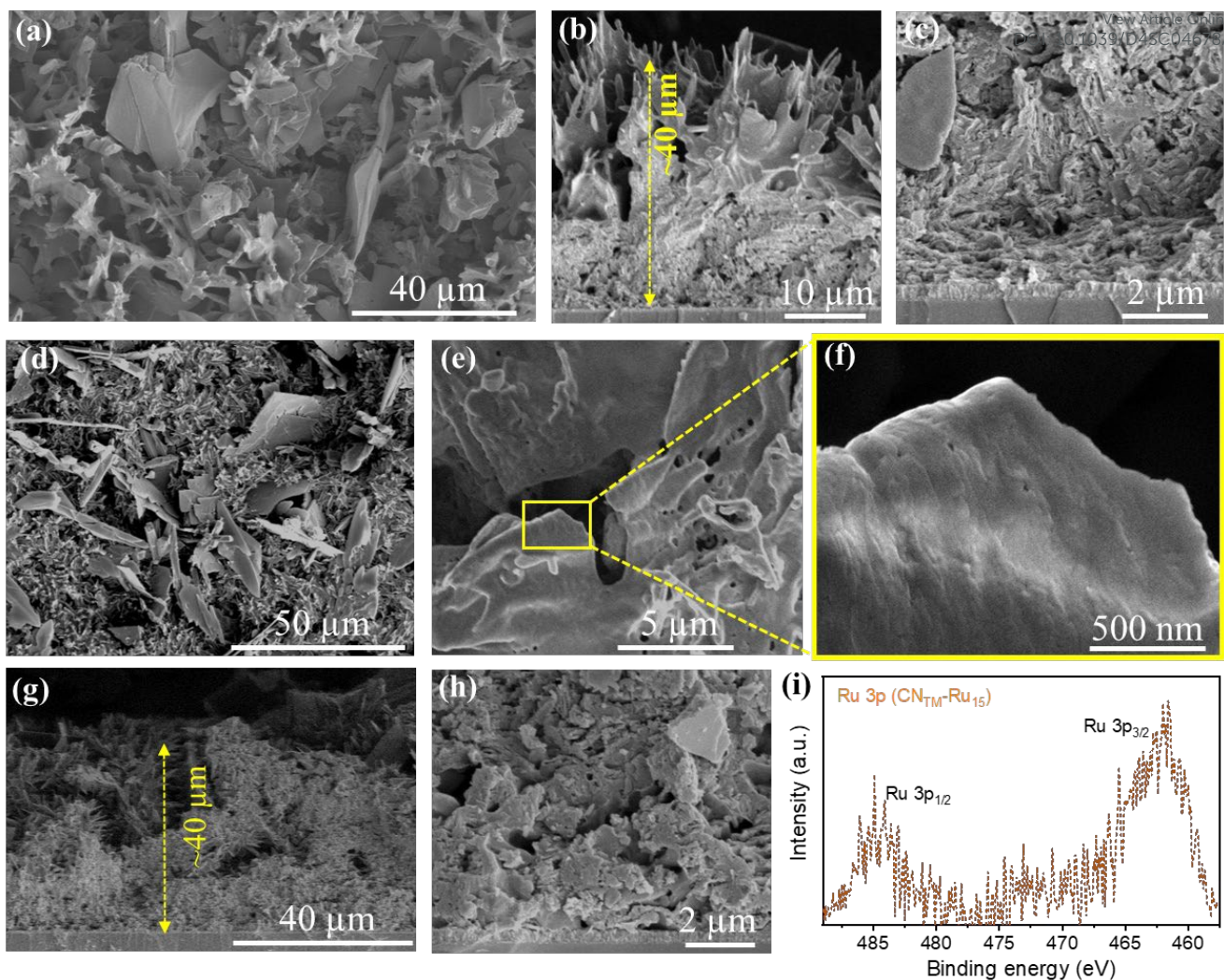


Fig. 3 (a) SEM image showing the morphology of the upper surface of the CN_{Tm} electrode. (b, c) Cross-sectional SEM images of CN_{Tm} electrodes at different magnifications. (d, e, f) Top-view of $\text{CN}_{\text{Tm}}\text{-Ru}_{15}$ at different magnifications. (g, h) Cross-sectional SEM images of $\text{CN}_{\text{Tm}}\text{-Ru}_{15}$ electrodes at different magnifications. (i) High-resolution Ru 3p XPS spectrum of a $\text{CN}_{\text{Tm}}\text{-Ru}_{15}$ film.

a thickness of 40–50 μm . The $\text{CN}_{\text{Tm}}\text{-Ru}_{15}$ film images (Fig. 3d–f) suggest the preservation of the porous sheet-like morphology, with a rough surface. The cross-section analysis (Fig. 3g–h) indicates an intimate contact between the film and substrate with film thickness similar to that of the CN_{Tm} film. Energy dispersive X-ray spectroscopy (EDS) confirms the presence of Ru in the $\text{CN}_{\text{Tm}}\text{-Ru}_{15}$ film (Fig. S5[†]). Moreover, the morphology of the $\text{CN}_{\text{Tm}}\text{-Ru}_{15}$ sample was examined using a high-angle annular dark-field scanning transmission electron microscope (HAADF-STEM), revealing the layered structure of the CN (see Fig. S6[†]). EDS mapping further confirms the presence and distribution of the Ru_{15} oligomer over the CN surface (Fig. S7[†]).

X-ray photoelectron spectroscopy (XPS) confirms the successful loading of Ru_{15} on CN_{Tm} film, showing the presence of C, N, and Ru in the $\text{CN}_{\text{Tm}}\text{-Ru}_{15}$ film (Fig. S8a[†]). The high-resolution XPS C 1s spectrum of CN_{Tm} film (Fig. S8b[†]) exhibits three peaks centered around 284.7 and 288.3 eV, assigned to C=O groups, sp^2 C–C bonding, and N–C=N bonding in the triazine units of carbon nitride, respectively. The high-resolution N 1s XPS curve shows three deconvoluted peaks attributed to C–

N=C, N–(C)₃, and C–N–H_x bond, respectively (Fig. S8c[†]).^{39,41,42} The deconvolution of the C 1s spectrum of the $\text{CN}_{\text{Tm}}\text{-Ru}_{15}$ sample reveals six peaks. The additional three peaks are ascribed to C–C=C (sp^2), N(sp^2)–C, and Ru 3d_{3/2} (overlapping with C 1s), respectively, originating from the Ru-oligomer (Fig. S8b[†]). The N 1s spectrum of $\text{CN}_{\text{Tm}}\text{-Ru}_{15}$ shows five deconvoluted peaks, where the additional two peaks are centered at 397.4 and 399.2 eV and originate from the Ru-oligomer (Fig. S8c[†]). High-resolution S 2p spectrum (Fig. S8d[†]) shows the peaks centered at 167.9 and 169.6 eV, ascribed to an S–H bond (S 2p_{3/2} and S 2p_{1/2}, respectively) in the CN film, which was prepared using a thiourea precursor as the S source.

It is noteworthy that the peaks related to C–N=C, N–(C)₃, and C–N–H_x bonds stemming from the carbon nitride have shifted to higher binding energies after modification with Ru_{15} due to the Ru oligomer/CN interaction. The high-resolution XPS Ru 3p spectrum of $\text{CN}_{\text{Tm}}\text{-Ru}_{15}$ film displays peaks in the 485–460 eV range, attributed to the presence of Ru(II) species (Fig. 3i).⁴³ Finally, inductively-coupled plasma optical emission spectroscopy (ICP-OES) elemental analysis for the $\text{CN}_{\text{Tm}}\text{-Ru}_{15}$



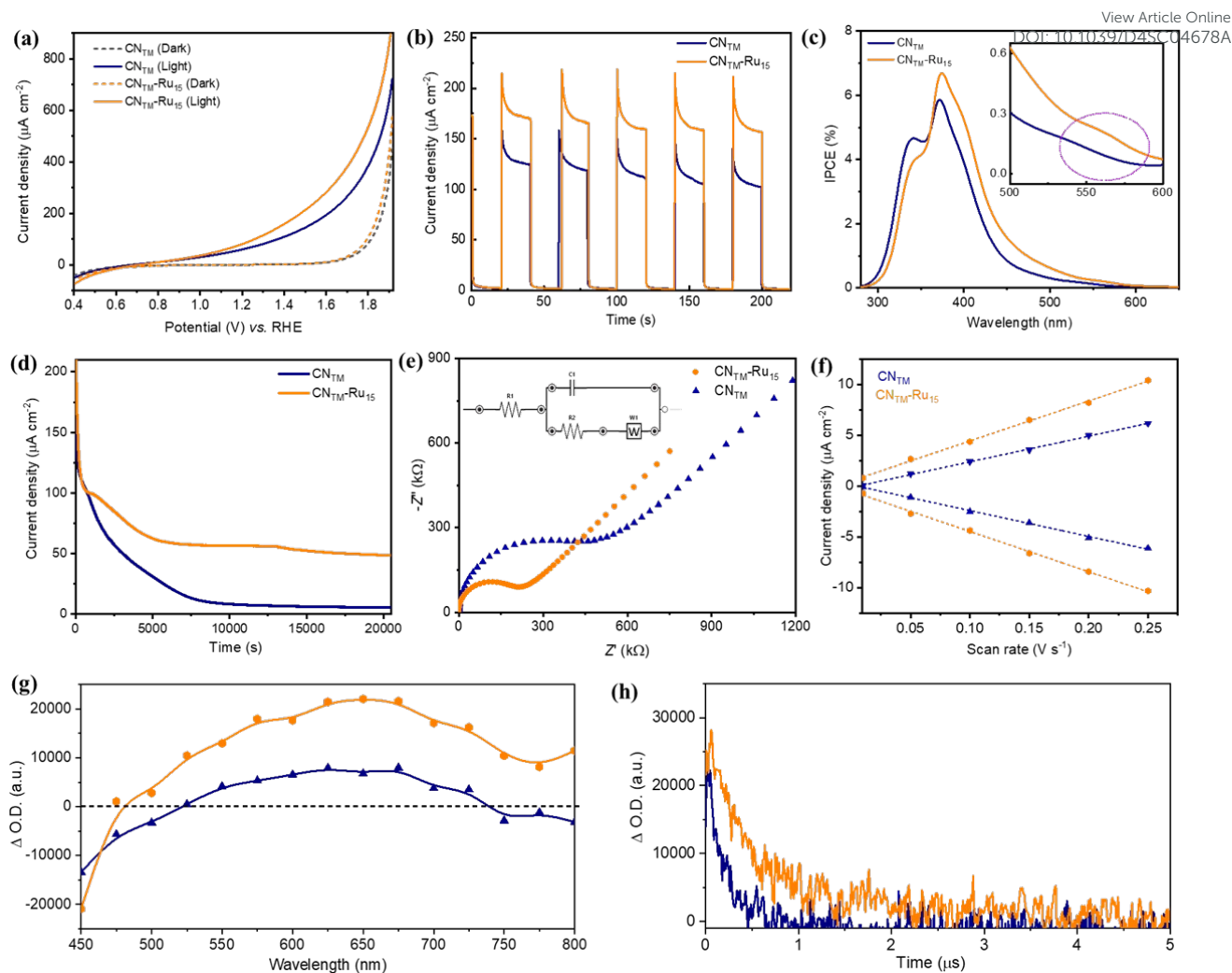


Fig. 4 (a) Linear sweep voltammetry (LSV) of CN_{Tm} and $\text{CN}_{\text{Tm-Ru15}}$ electrodes (phosphate buffer, pH 7) in the dark and under 1 sun illumination. (b) Chronoamperometry (current densities vs. time) of CN_{Tm} and $\text{CN}_{\text{Tm-Ru15}}$ electrodes in phosphate buffer (pH 7) at 1.23 V_{RHE} upon/off 1 sun illumination. (c) Incident photon-to-current conversion efficiency (IPCE) of the CN_{Tm} and $\text{CN}_{\text{Tm-Ru15}}$ film at different wavelengths (280–650 nm) in a phosphate buffer solution (pH 7) at 1.23 V_{RHE} . (d) Stability measurement (current density under continuous 1 sun illumination) of CN_{Tm} and $\text{CN}_{\text{Tm-Ru15}}$ electrodes in phosphate buffer (pH 7). (e) Nyquist plot of CN_{Tm} and $\text{CN}_{\text{Tm-Ru15}}$ films (fitted data shown). As an inset, the equivalent circuit used for fitting is shown, including a Warburg diffusion element (W); the R_{ct} value was obtained by fitting the semicircles of the Nyquist plots. (f) Cathodic and anodic charging current densities of CN films at 0 V vs. Ag/AgCl as a function of scan rate. (g) Transient absorption spectra of CN_{Tm} (blue triangles) and $\text{CN}_{\text{Tm-Ru15}}$ (orange hexagons) dispersions in MeCN and acquired at 250 ns. (h) Transient absorption decays of CN_{Tm} (blue) and $\text{CN}_{\text{Tm-Ru15}}$ (orange) dispersions in MeCN, monitored at 650 nm. The measurements were performed upon laser excitation at 355 nm under N_2 atmosphere. The CN_{Tm} and $\text{CN}_{\text{Tm-Ru15}}$ dispersions' UV-vis absorption was adjusted at identical values at the excitation wavelength (355 nm).

samples gives 6.5 μg of Ru per g of sample, that implies 64.3 nmols of Ru per g of $\text{CN}_{\text{Tm-Ru15}}$ (See Table S1[†]).

PEC measurements of CN_{Tm} and $\text{CN}_{\text{Tm-Ru15}}$ films were investigated in a three-electrode system under simulated 1 sun illumination in a $\text{NaH}_2\text{PO}_4/\text{Na}_2\text{HPO}_4$ buffer solution (pH 7, ionic-strength 0.1 M) as a supporting electrolyte. Linear sweep voltammetry (LSV) curves (Fig. 4a) of CN_{Tm} and $\text{CN}_{\text{Tm-Ru15}}$ films demonstrate a typical PEC behavior, with an onset potential of 0.55 V vs. RHE. Chronoamperometry measurements at 1.23 V vs. RHE (Fig. 4b) reveal that the incorporation of Ru_{15} leads to an improvement in the photocurrent densities of about 40%, from $130 \pm 8 \mu\text{A cm}^{-2}$ for the CN_{Tm} film to $180 \pm 10 \mu\text{A cm}^{-2}$ for the $\text{CN}_{\text{Tm-Ru15}}$ film both at an $E_{\text{app}} = 1.23$ V vs. RHE. This improvement is attributed to the synergy between the CN_{Tm}

and Ru_{15} anchored on the surface by $\text{CH}-\pi$ interactions, facilitating charge transfer and separation and the additional capacity of Ru_{15} to efficiently catalyze the water oxidation reaction.

The measured incident photon-to-current conversion efficiency (IPCE) of CN_{Tm} and $\text{CN}_{\text{Tm-Ru15}}$ films at several illumination wavelengths ranging from 280 to 650 nm is displayed in Fig. 4c. The IPCE values are in good agreement with the absorption spectra of the films. The IPCE value of $\text{CN}_{\text{Tm-Ru15}}$ film (6.7%) is higher than that of the CN_{Tm} film (5.8%) at 370 nm. In addition, the IPCE measurement reveals that $\text{CN}_{\text{Tm-Ru15}}$ film is photoactive at longer wavelengths, up to ~ 550 nm (inset of Fig. 4c), mainly due to the contribution of the Ru_{15} (Fig. S2[†]).



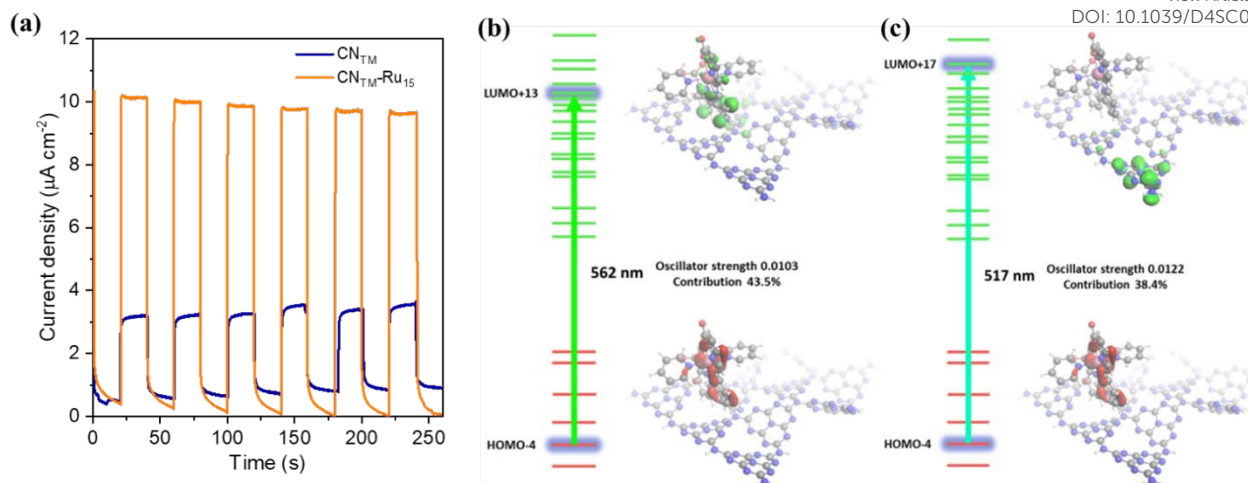


Fig. 5 (a) Chronoamperometry (current densities vs. time) of CN_{TM} and $\text{CN}_{\text{TM}}\text{-Ru}_{15}$ electrodes in phosphate buffer (pH 7) at 1.23 V vs. RHE under illumination using 510 nm band-pass filter (FWHM 10 nm). Calculated major contributions for electronic transition.

Notably, the incorporation of Ru_{15} into the CN_{TM} film significantly enhances the long-term stability. As shown in Fig. 4d, $\text{CN}_{\text{TM}}\text{-Ru}_{15}$ films in a neutral pH medium retain $\sim 35\%$ photocurrent density even after 5.5 h. In sharp contrast, the CN_{TM} film completely loses its photocurrent density ($\sim 96\%$) within 2 hours. Importantly, O_2 measurements indicate that most of the current is attributed to oxygen evolution and not to the self-oxidation of the CN layer. The $\text{CN}_{\text{TM}}\text{-Ru}_{15}$ generates O_2 with a rate of $0.014 \mu\text{mol cm}^{-2} \text{min}^{-1}$ (Fig. S9[†]) with Faradaic efficiency (FE) up to 89% after 20 min. Overall it implies a TON over 3000 after 5 h and a TOF of 0.4 s^{-1} (Table S2[†]).

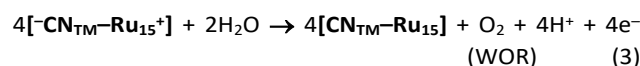
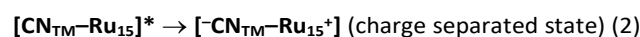
A comparison table for the PEC performance using metal oxides as WOCs co-catalyst with CN-based film is given in Table S3[†]. It is worth mentioning that the molecular hybrid material is superior in terms of FE for O_2 generation. It is also important to mention here that the amount of used Ru is in the range of micrograms of Ru per g of sample. This generally implies a loading of catalyst 4 to 6 orders of magnitude lower^{34,35} than related examples using Co, Ni, or Fe oxides.^{44,45}

The $\text{CN}_{\text{TM}}\text{-Ru}_{15}$ film after the stability experiment was examined using PXRD, XPS and SEM (Fig. S10[†]), revealing minimal alterations in the film's structure and morphology. The improved durability of the $\text{CN}_{\text{TM}}\text{-Ru}_{15}$ film is associated with better charge separation and the high OER catalytic activity of the Ru_{15} . We analyzed the charge transfer kinetics behavior of CN_{TM} and $\text{CN}_{\text{TM}}\text{-Ru}_{15}$ films using electrochemical impedance spectroscopy (EIS) and transient absorption spectroscopy (TAS) to elucidate the activity improvement. The EIS experiments (Fig. 4e, Fig. S11[†]) disclosed lower charge transfer resistance ($R_{\text{ct}} = 250 \text{ k}\Omega$) for $\text{CN}_{\text{TM}}\text{-Ru}_{15}$ film than for CN_{TM} alone ($470 \text{ k}\Omega$), implying better hole transfer to the solution. An increased electrochemically active surface area (ECSA) is shown in Fig. 4f and S12[†], indicating more active sites for water oxidation after modification with Ru_{15} oligomer.

TAS measurements of CN_{TM} and $\text{CN}_{\text{TM}}\text{-Ru}_{15}$ dispersions in MeCN upon 355 nm laser excitation further confirmed the

improved photo-induced charge transfer kinetics in the presence of the Ru_{15} . The TA spectrum of CN_{TM} (Fig. 4g) exhibits a negative feature up to ca. 525 nm, due to the bleaching of the ground state absorption of CN_{TM} . The detected positive signal from 525 to 750 nm indicates the presence of excited states absorbing in the visible region, as previously reported for related CN materials. The TA spectrum of $\text{CN}_{\text{TM}}\text{-Ru}_{15}$ presents similar features with higher signal intensity. Still, it exhibits an extended transient absorption in the NIR region (750–800 nm) due to the Ru_{15} incorporation. It is worth noticing that the increase in the positive signal intensity for $\text{CN}_{\text{TM}}\text{-Ru}_{15}$ is proportional to an enhancement in photo-induced charge carriers, in good agreement with the photocurrent and IPCE measurements, indicating a more efficient charge separation in $\text{CN}_{\text{TM}}\text{-Ru}_{15}$ compared to CN_{TM} . These positive signals are attributed to photo-generated electrons in CN_{TM} and $\text{CN}_{\text{TM}}\text{-Ru}_{15}$. Hole quenching experiments using MeOH as a sacrificial electron donor (Fig. S13[†]) confirm that the electrons are the main charge carriers detected in these experimental conditions.

The TA decays of CN_{TM} and $\text{CN}_{\text{TM}}\text{-Ru}_{15}$ at 650 nm (Fig. 4h) reveal an almost one magnitude order longer electron half-life of the $\text{CN}_{\text{TM}}\text{-Ru}_{15}$ ($1.60 \mu\text{s}$) vs. CN_{TM} ($0.24 \mu\text{s}$) thanks to a better charge separation and thus lower recombination rates. This agrees with the mechanism proposed in Equations 1–3:



where the introduction of supramolecularly-bonded Ru_{15} on the CN_{TM} layer results in an enhanced charge separated state (Equation 2), mainly thanks to fast hole extraction from the CN_{TM} to the Ru_{15} , followed by water oxidation reaction (WOR) (Equation 3). The final assembly is thus overall leading to better



photoactivity at longer wavelengths and better electron collection.

Furthermore, additional photocurrent measurements were performed using 510 nm band-pass filter (FWHM 10 nm) for both the electrodes as presented in Fig. 5a, showing a photocurrent enhancement of approx. 3.2 times higher in case of **CN_{TM}-Ru₁₅** compared to **CN_{TM}** due to the presence of the molecular catalyst. This points out the behavior of the **Ru₁₅** as both light absorber and catalyst.⁴⁶ To gain some insights on the processes occurring upon light excitation of the system, we computed the absorption spectra by means of TD-DFT of the model hybrid **CN_{Red}-Ru₂**, and the results are shown in Fig. 5 and Fig. S14–S22†. Two transitions are displayed in the figure, one at 562 nm (Fig. 5b) that is mainly intramolecular involving the Ru catalyst, which later on can further transfer an electron to the valence band of the **CN_{Red}** moiety, resembling the typical Grätzel's dye-sensitized solar cells based on TiO₂ and [Ru(bpy)₃]²⁺.^{47,48} A second excitation at 517 nm, shown in Fig. 5c, would involve a direct charge transfer from the Ru center into the valence band of **CN_{Red}**.

Conclusions

In this work, we introduced a new molecular hybrid material **CN_{TM}-Ru₁₅** based on the anchoring of a highly active molecular water oxidation catalyst on **CN_{TM}** photoanode. The successful deposition of **Ru₁₅** oligomer on polymeric carbon nitride photoanodes (**CN_{TM}**) through CH- π interactions enables good photoelectrochemical water-splitting activity at neutral pH, enhanced long-term stability and high FE (> 89%) for oxygen production. Detailed structural, photoelectrochemical, and mechanistic studies reveal that the **Ru₁₅** markedly improves charge separation and hole extraction kinetics, enabling efficient water oxidation. Furthermore, the **Ru₁₅** oligomer leads to better light harvesting, higher electrochemical surface area, and improved electronic conductivity. The optimized **CN_{TM}-Ru₁₅** film demonstrates a photocurrent density of $180 \pm 10 \mu\text{A cm}^{-2}$ with 89% FE for oxygen evolution, good stability up to 5 h, and IPCE values up to 6.7%. The amount of Ru-based catalyst loaded on the surface that represents only 6.5 ppm of the electrode composition and leads to TONs in the range of 3300 and a TOF of 0.4 s^{-1} . Furthermore, we have also shown that in the **CN_{TM}-Ru₁₅** hybrid material the Ru centers act both as catalyst and as photoabsorber.

Finally, the present work is an example of the positive synergy that can be obtained with the proper utilization of a molecular-based catalyst and a polymeric organic absorber.

Data availability

The data supporting this article have been included as part of the ESI.† The underlying raw data is available on request to the authors.

Author contributions

S.M. performed most of the experiments, analyzed the data, and wrote the initial draft of the manuscript. M.S. synthesized and characterized the **Ru₁₅** oligomer and participated in manuscript writing. M.N. performed the DFT calculations and analysis. J.A. and H.G. performed the TAS measurements. M.S.C., C.B., and M.G.S. took part in the DFT study. M.V. took part in analysis, SEM imaging, and manuscript editing. M.S. and A.L. supervised the study, co-wrote and reviewed the paper, and acquired funding. All the authors discussed the results and reviewed the manuscript. All authors have given approval to the final version of the manuscript.

Conflicts of interest

There are no conflicts to declare.

Acknowledgements

This project has received funding from the European Research Council (ERC) under the European Union's Horizon 2020 research and innovation program (Grant Agreement No. 849068). This work was also partially supported by the Israel Science Foundation (ISF), Grant No. 601/21. MS and MN acknowledge Ministerio de Ciencia e Innovación (MICINN) for the grants PRE2020-093789 and PRE2020-093521 respectively. CB gratefully acknowledges MICINN/AEI/10.13039/501100011033 for project PID2020-112806RB-I00 and CEX2019-000925-S, the ICIQ Foundation and the CERCA program of the Generalitat de Catalunya for funding. HG thanks MICINN (CEX-2021-001230-S and PDI2021-0126071-OB-CO21 funded by MCIN/AEI/10.13039/501100011033), Generalitat Valenciana (Prometeo 2021/038 and Advanced Materials programme Graphica MFA/2022/023 with funding from European Union Next Generation EU PRTR-C17.I1). JA thanks the MICINN for a Ramon y Cajal research associate contract (RYC2021-031006-I funded by MCIN/AEI/10.13039/501100011033 and by "European Union Next Generation EU/PRTR), and the financial support (PID2022-141099OA-I00 funded by MICINN/AEI/10.13039/501100011033 and, by "European Union Next Generation EU/PRTR). AL acknowledges MICINN through project PID2022-140143OB-I00, Generalitat de Catalunya for the project 2017 SGR 1631 and Severo Ochoa (CEX2019-000925-S).

References

- 1 M. Volokh, G. Peng, J. Barrio and M. Shalom, *Angew. Chem. Int. Ed.*, 2019, **58**, 6138–6151.
- 2 N. P. Dharmarajan, D. Vidyasagar, J.-H. Yang, S. N. Talapaneni, J. Lee, K. Ramadass, G. Singh, M. Fawaz, P. Kumar and A. Vinu, *Adv. Mater.*, 2023, **36**, 2306895.
- 3 X. Fan, Z. Wang, T. Lin, D. Du, M. Xiao, P. Chen, S. A. Monny, H. Huang, M. Lyu, M. Lu and L. Wang, *Angew. Chem. Int. Ed.*, 2022, **61**, e202204407.



- 4 G. Peng, J. Albero, H. Garcia and M. Shalom, *Angew. Chem. Int. Ed.*, 2018, **57**, 15807–15811.
- 5 J. Zhang, J. Zhang, C. Dong, Y. Xia, L. Jiang, G. Wang, R. Wang and J. Chen, *Small*, 2023, **19**, 2208049.
- 6 T. H. Jeon, C. Park, U. Kang, G. Moon, W. Kim, H. Park and W. Choi, *Appl. Catal. B Environ.*, 2024, **340**, 123167.
- 7 M. Fawaz, R. Bahadur, N. Panangattu Dharmarajan, J.-H. Yang, C. I. Sathish, A. M. Sadanandan, V. Perumalsamy, G. Singh, X. Guan, P. Kumar and A. Vinu, *Carbon N. Y.*, 2023, **214**, 118345.
- 8 J. Qin, J. Barrio, G. Peng, J. Tzadikov, L. Abisdri, M. Volokh and M. Shalom, *Nat. Commun.*, 2020, **11**, 4701.
- 9 L. Jiang, X. Yuan, Y. Pan, J. Liang, G. Zeng, Z. Wu and H. Wang, *Appl. Catal. B Environ.*, 2017, **217**, 388–406.
- 10 S. Mondal, G. Mark, L. Abisdri, J. Li, T. Shmila, J. Tzadikov, M. Volokh, L. Xing and M. Shalom, *Mater. Horizons*, 2023, **10**, 1363–1372.
- 11 Y. Yang, S. Wang, Y. Jiao, Z. Wang, M. Xiao, A. Du, Y. Li, J. Wang and L. Wang, *Adv. Funct. Mater.*, 2018, **28**, 1805698.
- 12 S. Mondal, G. Mark, A. Tashakory, M. Volokh and M. Shalom, *J. Mater. Chem. A*, 2024, **12**, 11502–11510.
- 13 T. Shmila, S. Mondal, S. Barzilai, N. Karjule, M. Volokh and M. Shalom, *Small*, 2023, **19**, 2303602.
- 14 F. Li, X. Yue, Y. Liao, L. Qiao, K. Lv and Q. Xiang, *Nat. Commun.*, 2023, **14**, 3901.
- 15 N. Karjule, C. Singh, J. Barrio, J. Tzadikov, I. Liberman, M. Volokh, E. Palomares, I. Hod and M. Shalom, *Adv. Funct. Mater.*, 2021, **31**, 2101724.
- 16 Y. Hou, F. Zuo, A. P. Dagg, J. Liu and P. Feng, *Adv. Mater.*, 2014, **26**, 5043–5049.
- 17 W. Zhang, J. Albero, L. Xi, K. M. Lange, H. Garcia, X. Wang and M. Shalom, *ACS Appl. Mater. Interfaces*, 2017, **9**, 32667–32677.
- 18 R. Gong, D. Mitoraj, D. Gao, M. Mundsziinger, S. Sorsche, U. Kaiser, C. Streb, R. Beranek and S. Rau, *Adv. Sustain. Syst.*, 2022, **6**, 2100473.
- 19 I. Cesar, A. Kay, J. A. Gonzalez Martinez and M. Grätzel, *J. Am. Chem. Soc.*, 2006, **128**, 4582–4583.
- 20 Z. Wang, Y. Gu, L. Zheng, J. Hou, H. Zheng, S. Sun and L. Wang, *Adv. Mater.*, 2022, **34**, 2106776.
- 21 J. Liu, Z. Luo, X. Mao, Y. Dong, L. Peng, D. Sun-Waterhouse, J. V Kennedy and G. I. N. Waterhouse, *Small*, 2022, **18**, 2204553.
- 22 B. Liu, X. Wang, Y. Zhang, L. Xu, T. Wang, X. Xiao, S. Wang, L. Wang and W. Huang, *Angew. Chem. Int. Ed.*, 2023, **62**, e202217346.
- 23 Z. Zhang, X. Huang, B. Zhang and Y. Bi, *Energy Environ. Sci.*, 2022, **15**, 2867–2873.
- 24 J. Lin, X. Han, S. Liu, Y. Lv, X. Li, Y. Zhao, Y. Li, L. Wang and S. Zhu, *Appl. Catal. B Environ.*, 2023, **320**, 121947.
- 25 A. Tashakory, N. Karjule, L. Abisdri, M. Volokh and M. Shalom, *Adv. Sustain. Syst.*, 2021, **5**, 2100005.
- 26 J. Xia, N. Karjule, L. Abisdri, M. Volokh and M. Shalom, *Chem. Mater.*, 2020, **32**, 5845–5853.
- 27 P. Garrido-Barros, C. Gimbert-Suriñach, R. Matheu, X. Sala and A. Llobet, *Chem. Soc. Rev.*, 2017, **46**, 6088–6098.
- 28 M. Gil-Sepulcre and A. Llobet, *Nat. Catal.*, 2022, **5**, 79–82.
- 29 N. Vereshchuk, M. Gil-Sepulcre, A. Ghaderian, J. Holub, C. Gimbert-Suriñach and A. Llobet, *Chem. Soc. Rev.*, 2023, **52**, 196–211.
- 30 R. Matheu, M. Z. Ertem, J. Benet-Buchholz, E. Coronado, V. S. Batista, X. Sala and A. Llobet, *J. Am. Chem. Soc.*, 2015, **137**, 10786–10795.
- 31 R. Matheu, I. A. Moreno-Hernandez, X. Sala, H. B. Gray, B. S. Brunshwig, A. Llobet and N. S. Lewis, *J. Am. Chem. Soc.*, 2017, **139**, 11345–11348.
- 32 J. Creus, R. Matheu, I. Peñafiel, D. Moonshiram, P. Blondeau, J. Benet-Buchholz, J. García-Antón, X. Sala, C. Godard and A. Llobet, *Angew. Chem. Int. Ed.*, 2016, **55**, 15382–15386.
- 33 S. Grau, S. Berardi, A. Moya, R. Matheu, V. Cristino, J. J. Vilatela, C. A. Bignozzi, S. Caramori, C. Gimbert-Suriñach and A. Llobet, *Sustain. Energy Fuels*, 2018, **2**, 1979–1985.
- 34 M. A. Hoque, M. Gil-Sepulcre, A. de Aguirre, J. A. A. W. Elemans, D. Moonshiram, R. Matheu, Y. Shi, J. Benet-Buchholz, X. Sala, M. Malfois, E. Solano, J. Lim, A. Garzón-Manjón, C. Scheu, M. Lanza, F. Maseras, C. Gimbert-Suriñach and A. Llobet, *Nat. Chem.*, 2020, **12**, 1060–1066.
- 35 M. Gil-Sepulcre, J. O. Lindner, D. Schindler, L. Velasco, D. Moonshiram, O. Rüdiger, S. DeBeer, V. Stepanenko, E. Solano, F. Würthner and A. Llobet, *J. Am. Chem. Soc.*, 2021, **143**, 11651–11661.
- 36 D. Schindler, M. Gil-Sepulcre, J. O. Lindner, V. Stepanenko, D. Moonshiram, A. Llobet and F. Würthner, *Adv. Energy Mater.*, 2020, **10**, 2002329.
- 37 R. S. Roy, S. Mondal, S. Mishra, M. Banoo, L. Sahoo, A. Kumar, C. P. Vinod, A. K. De and U. K. Gautam, *Appl. Catal. B Environ.*, 2023, **322**, 122069.
- 38 G. Mark, S. Mondal, M. Volokh, J. Xia and M. Shalom, *Sol. RRL*, 2022, **6**, 2200834.
- 39 S. Mondal, L. Sahoo, Y. Vaishnav, S. Mishra, R. S. Roy, C. P. Vinod, A. K. De and U. K. Gautam, *J. Mater. Chem. A*, 2020, **8**, 20581–20592.
- 40 N. Karjule, J. Barrio, L. Xing, M. Volokh and M. Shalom, *Nano Lett.*, 2020, **20**, 4618–4624.
- 41 Y. Hou, Y. Zhu, Y. Xu and X. Wang, *Appl. Catal. B Environ.*, 2014, **156–157**, 122–127.
- 42 Q. Zhang, X. Chen, Z. Yang, T. Yu, L. Liu and J. Ye, *ACS Appl. Mater. Interfaces*, 2022, **14**, 3970–3979.
- 43 M. K. Awasthi, R. K. Rai, S. Behrens and S. K. Singh, *Catal. Sci. Technol.*, 2021, **11**, 136–142.
- 44 J. Ma, X. Bai, W. He, S. Wang, L. Li, H. Chen, T. Wang, X. Zhang, Y. Li and L. Zhang, *Chem. Commun.*, 2019, **55**, 12567–12570.
- 45 M. Volokh and M. Shalom, *Ann. N. Y. Acad. Sci.*, 2023, **1521**, 5–13.
- 46 I. N. Cloward, T. Liu, J. Rose, T. Jurado, A. G. Bonn, M. B. Chambers, C. L. Pitman, M. A. Ter Horst and A. J. M. Miller, *Nat. Chem.*, 2024, 1–8.
- 47 G. Li, A. Yella, D. G. Brown, S. I. Gorelsky, M. K. Nazeeruddin, M. Grätzel, C. P. Berlinguette and M. Shatruk, *Inorg. Chem.*, 2014, **53**, 5417–5419.
- 48 M. Grätzel, *Acc. Chem. Res.*, 2009, **42**, 1788–1798.



Data Availability Statement

All data on which this publication is based appears either in the main text or in the ESI.† The underlying raw data is available on request to the authors.

ESI† includes materials, characterization, PEC and electrochemical measurements, detailed synthesis procedures of the Ru₁₅ oligomer, photoelectrodes, computational details, Figures, calculations, tables and detailed data of the theoretical part.

